

Nano-imaging of intersubband transitions in van der Waals quantum wells

Peter Schmidt¹, Fabien Vialla^{1,2}, Simone Latini^{3,4}, Mathieu Massicotte¹, Klaas-Jan Tielrooij¹, Stefan Mastel⁵, Gabriele Navickaite¹, Mark Danovich⁶, David A. Ruiz-Tijerina⁶, Celal Yelgel⁶, Vladimir Fal'ko⁶, Kristian S. Thygesen⁷, Rainer Hillenbrand^{5,7} and Frank H. L. Koppens^{1,8*}

The science and applications of electronics and optoelectronics have been driven for decades by progress in the growth of semiconducting heterostructures. Many applications in the infrared and terahertz frequency range exploit transitions between quantized states in semiconductor quantum wells (intersubband transitions). However, current quantum well devices are limited in functionality and versatility by diffusive interfaces and the requirement of lattice-matched growth conditions. Here, we introduce the concept of intersubband transitions in van der Waals quantum wells and report their first experimental observation. Van der Waals quantum wells are naturally formed by two-dimensional materials and hold unexplored potential to overcome the aforementioned limitations—they form atomically sharp interfaces and can easily be combined into heterostructures without lattice-matching restrictions. We employ near-field local probing to spectrally resolve intersubband transitions with a nanometre-scale spatial resolution and electrostatically control the absorption. This work enables the exploitation of intersubband transitions with unmatched design freedom and individual electronic and optical control suitable for photodetectors, light-emitting diodes and lasers.

The nanoscale confinement of charge carriers gives rise to a rich variety of physical phenomena that are not present in bulk materials and lies at the heart of many modern optoelectronic applications^{1–4}. One striking feature is that confinement leads to quantized energy levels, whose energy spacing increases with spatial confinement. Charge carriers can be confined in three dimensions (0D quantum dots⁵), in two dimensions (1D quantum wires⁶) or in one dimension (2D quantum wells). The last is arguably the most well-known example and has led to the development of quantum well infrared photodetectors⁷ and quantum cascade lasers⁸ for mid-infrared to terahertz wavelengths. These devices rely on the transitions of electrons (or holes) between the quantized states—intersubband transitions^{9–11}—of a semiconductor quantum well. In contrast to interband transitions, these intraband transitions exhibit very large oscillator strengths close to unity⁹. At present, state-of-the-art quantum wells are typically grown by molecular beam epitaxy of different III–V semiconductor alloys. This technology suffers from fundamental material limitations: strict lattice matching conditions limit the available material combinations and the thermal growth causes atomic diffusion and increases the interface roughness, which restricts the performances of actual devices¹².

Recently, 2D materials and their heterostructures have emerged as a promising platform for electronic and optoelectronic applications^{13–17}, with particular interest for the 2D semiconductors such as transition metal dichalcogenides (TMDs). Studies on TMDs encapsulated in hexagonal boron nitride (h-BN) reveal appealing electrical properties, such as mobilities $>30,000\text{ cm}^2\text{ V}^{-1}\text{ s}^{-1}$ of MoS₂ (ref. ¹⁸) and the demonstration of the quantum Hall effect in WSe₂ (ref. ¹⁹) and InSe (ref. ²⁰). Unique optical features have been reported, which include spin–valley locking²¹, the valley Hall effect²², near-unity excitonic reflection^{23,24} and photoluminescence close to the homogeneous linewidth^{25,26}. All of these optical phenomena in monolayer 2D materials arise from interband electronic transitions.

However, few-layer 2D materials also form natural quantum wells—van der Waals quantum wells—in which charge carriers are quantum confined to the nanoscale in one dimension and it is therefore natural to expect intersubband transitions to occur. Cross-section transition electron microscopy images of van der Waals heterostructures have demonstrated defect-free and atomically sharp interfaces^{14,18,27}, which enables the formation of ideal quantum wells, free of diffusive inhomogeneities. Furthermore, van der Waals quantum wells do not require epitaxial growth on a lattice-matched substrate and can therefore be easily isolated and coupled to other electronic systems, such as a Si complementary metal–oxide semiconductor (CMOS), or optical systems, such as cavities and waveguides. Finally, by assembling van der Waals quantum wells into heterostructures, combined with metals or semimetals such as graphene, it is possible to electrically contact each quantum well individually²⁸, which allows for in situ tuning of resonances and interactions as well as facile carrier injection.

Here we introduce the concept of intersubband transitions in van der Waals quantum wells, report their experimental observation by near-field imaging with nanometre-scale resolution, and provide detailed theoretical calculations. We probed the transitions between the quantized states within both the valence and the conduction band by investigating the mid-infrared optical response of doped TMDs. The TMDs were exfoliated on a Si/HfO₂ substrate (specifically chosen to avoid contributions from substrate phonons) and electron or hole doping was induced by applying a gate voltage between the Si and TMD. Each investigated flake comprised several terraces of different layer number N in which charge carriers are quantum confined in the out-of-plane direction within the TMD flake, as illustrated in Fig. 1a. As the quantum wells are not buried inside any material, we can perform scattering scanning near-field optical microscopy (s-SNOM)²⁹ as an innovative measurement approach to spectrally resolve

¹ICFO - Institut de Ciències Fotòniques, The Barcelona Institute of Science and Technology, Castelldefels (Barcelona), Spain. ²Institut Lumière Matière UMR5306, Université Claude Bernard Lyon1 - CNRS, Villeurbanne, France. ³Center for Atomic-scale Materials Design, Technical University of Denmark, Kongens Lyngby, Denmark. ⁴Max Planck Institute for the Structure and Dynamics of Matter, Hamburg, Germany. ⁵CIC nanoGUNE Consolider, Donostia-San Sebastián, Spain. ⁶National Graphene Institute, University of Manchester, Manchester, UK. ⁷IKERBASQUE, Basque Foundation for Science, Bilbao, Spain. ⁸ICREA-Institució Catalana de Recerca i Estudis Avançats, Barcelona, Spain. *e-mail: frank.koppens@icfo.eu

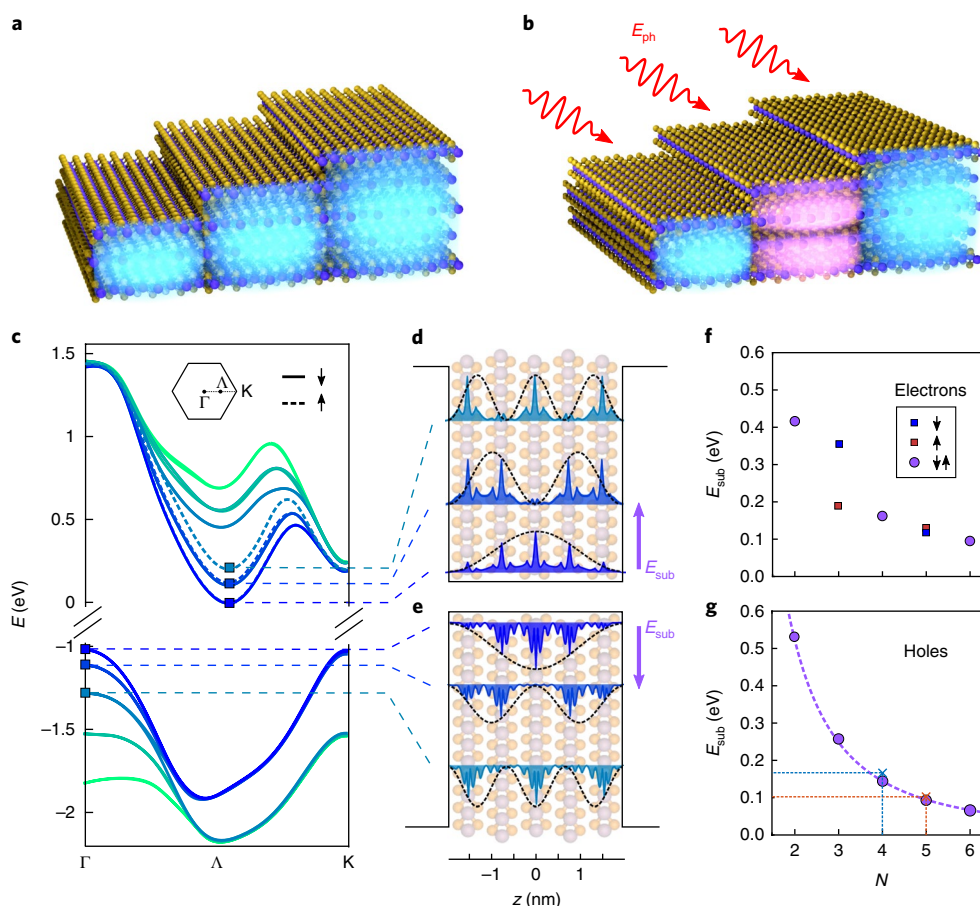


Fig. 1 | Van der Waals quantum wells—concept and theory. **a**, Schematic illustration of charge carriers (blue) confined within a TMD flake that consists of different thicknesses. **b**, On light excitation with a photon energy E_{ph} and an out-of-plane polarization, charge carriers can be excited from the ground state to the first excited state (pink) if the intersubband transition energy for a given thickness is resonant with E_{ph} . **c**, Ab initio DFT band structure calculations for a $N=5$ 2H-WSe₂ crystal. Shown are the five highest valence bands and the five lowest conduction bands, displayed along the Γ -K axis of the hexagonal Brillouin zone, as indicated in the inset. Spin-orbit coupling leads to an additional splitting of the conduction bands. The lowest three conduction bands can be assigned to spin down (up) and are marked by solid (dashed) lines. **d,e**, Calculated out-of-plane wavefunctions for a WSe₂ crystal with $N=5$ at the points in the Brillouin zone indicated in **c**. **d** shows the electron wave functions of the three lowest conduction bands at the Λ point, and **e** shows the hole wavefunctions of the three highest valence bands at the Γ point. Dashed lines represent the envelope functions assuming a perfect, infinitely deep square well potential. **f,g**, Calculated transition energies E_{sub} from the first to the second subband (purple arrows in **d** and **e**) as a function of N for electrons in the conduction band (**f**) and holes in the valence band (**g**). Blue (red) squares correspond to transitions between the spin down (up) polarized subbands, whereas purple circles correspond to transitions between spin-degenerate subbands. The purple dashed line is a fit to the spin-degenerate hole transitions using the modified infinite square well model (equation (1)) and yielded $\nu=0.09$. The crosses in **g** represent the measured transition energies.

intersubband absorption resonances with a spatial resolution below 20 nm. We spectrally resolved intersubband resonances for the different quantum well thicknesses within a single TMD flake by varying the illumination photon energy, as schematically depicted in Fig. 1b. Furthermore, we demonstrated the in situ control of the intersubband absorption strength by electrostatically tuning the charge carrier density of the TMD flake. Finally, to show the versatility of intersubband transitions in 2D materials, we demonstrated intersubband absorption in both valence and conduction bands within a single device.

Intersubband transition theory in van der Waals materials

First, we lay the theoretical framework for intersubband transitions in van der Waals quantum wells³⁰. Figure 1c shows the band structure of a 2H-WSe₂ crystal with layer number $N=5$, obtained by using ab initio density functional theory (DFT) calculations that include spin-orbit coupling. We confirmed the validity of our calculations by using two different, independent approaches

(Supplementary Section I gives more details). The calculations revealed the splitting of the lowest conduction (highest valence) band into several subbands. In contrast to monolayer TMD crystals, in which both band edges appear at the K points of the Brillouin zone³¹, few-layer WSe₂ has the valence band edge at the Γ point, and the conduction band edge at the Λ points, which are located close to the middle of the Γ -K segments in the Brillouin zone^{32,33}. This change in the characteristics of the band structure is determined by a strong overlap between the Γ and Λ point wavefunctions in neighbouring monolayers, which also determines the z -axis (out-of-plane) effective mass and the k_z dispersion in the bulk layered crystal³³. For the edge of the valence band, which appears at the 3D Γ point in 2H-WSe₂, we can approximate the dispersion of holes as $E \approx \frac{\hbar^2 k_z^2}{2m_z} + \frac{\hbar^2 k_{xy}^2}{2m_{xy}}(1 + \zeta k_z^2)$, where $m_z \approx 1.08 m_e$ and $m_{xy} \approx 0.7 m_e$ are the out-of-plane and in-plane effective masses obtained by fitting the bulk dispersion, \hbar is the reduced Planck constant, k_{xy} is the in-plane wavevector and $\zeta \approx -5.45 \text{ \AA}^2$ is an anisotropic non-parabolicity factor (Supplementary Section I.2 gives details).

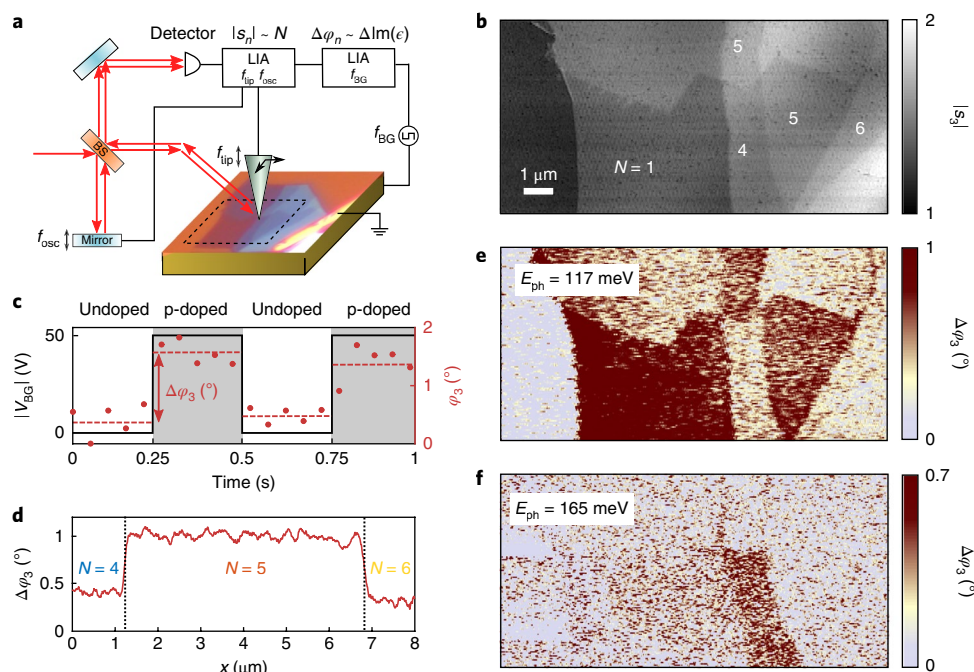


Fig. 2 | Measurement set-up and spatial absorption maps of a terraced WSe₂ flake. **a**, Real colour microscope image of the WSe₂ flake and schematic illustration of the s-SNOM (NeasNOM from Neaspec GmbH) measurement set-up. A mid-infrared laser beam is divided into two paths by a beam splitter (BS) for interferometric detection: one path is reflected by a mirror that oscillates with $f_{\text{osc}} \approx 300$ Hz, and the other beam is focused on the apex of a metallized AFM tip that oscillates with $f_{\text{tip}} \approx 250$ kHz, where it interacts with the sample in the near field. The back-scattered light carries information about the sample permittivity at the illumination photon energy E_{ph} . Both beams are recombined and detected by a cooled HgCdTe detector. To suppress the large background of light that is reflected from the AFM tip without interacting with the sample, the signal is evaluated at sidebands (which arise due to the mirror oscillation with f_{osc}) of higher harmonics n of f_{tip} by a built-in lock-in amplifier (LIA)⁵². Due to the interferometric detection, the recorded signal s_n is complex and for our specific system of a thin WSe₂ flake on top of a thick substrate, $|s_n|$ increases monotonically with the number of layers N of the WSe₂ flake (Supplementary Section III). s_n is further modulated by applying a square wave backgate voltage V_{BG} with frequency f_{BG} ($f_{\text{BG}} \ll f_{\text{osc}} \ll f_{\text{tip}}$) to the Si substrate, which thus modulates the doping of the WSe₂ flake. The change in phase of s_n with doping, $\Delta\varphi_n$, is proportional to the change in the imaginary part of the permittivity of WSe₂, $\Delta\text{Im}(\epsilon_{\text{WSe}_2})$. **b**, Spatial map of $|s_3|$ in arbitrary units obtained by scanning the AFM tip over the area of the flake marked by the dashed lines in **a**. Different layer numbers can be identified by their optical signal and are indicated in the map. **c**, Time trace of the modulated backgate voltage $|V_{\text{BG}}|$ (black solid line) and the corresponding phase of the third harmonic detector signal φ_3 (red dots). Data were obtained for $E_{\text{ph}} = 117$ meV with $f_{\text{BG}} = 1.9$ Hz in the resonant $N = 5$ layer of a WSe₂ flake. The dashed red lines indicate the average of φ_3 for when the flake is p-doped or charge neutral. The difference between these averages corresponds to $\Delta\varphi_3$. **d**, $\Delta\varphi_3$ on the same flake as in **c**, which contains terraces of different N . The data were obtained at $E_{\text{ph}} = 117$ meV by averaging ten identical line scans to increase the signal/noise ratio. **e**, Spatial map of $\Delta\varphi_3$ obtained during the same scan as shown in **b** with $E_{\text{ph}} = 117$ meV. Higher values of $\Delta\varphi_3$ correspond to higher absorption. **f**, Same as **e**, but for $E_{\text{ph}} = 165$ meV.

The splitting of the bands corresponds to the quantized states in the quantum well. The wavenumbers for these standing waves in the z -direction are determined by the boundary conditions $[\pm\nu d \partial_z \psi + \psi]_{z=\pm Nd/2} = 0$, with a monolayer thickness d and a phenomenological parameter ν (Supplementary Section I.2 gives details) for the hole wavefunction $\psi(z)$ at the top and bottom interfaces ($z = \pm Nd/2$). Figure 1d,e shows these (Λ and Γ point) out-of-plane wavefunctions for electrons and holes, respectively, which represent a periodic modulation with the same periodicity as the atomic potential multiplied by an envelope function. The boundary conditions give us $k_z = \pi j / (N + 2\nu)d$, with the subband index j . The energy of the $j = 1 \rightarrow j = 2$ intersubband transition in a lightly p-doped film is then given by modified infinite square well transition energies:

$$E_{\text{sub}} = E_{j=2} - E_{j=1} \approx \frac{1}{(N + 2\nu)^2} \frac{3\hbar^2 \pi^2}{2m_z d^2} \quad (1)$$

This fits very well with the transition energies obtained from the DFT results, shown in Fig. 1f,g. We note that for electrons, however,

an additional splitting of the transition energies for odd N occurs due to spin-orbit interactions.

Experimental set-up and spatially resolved measurements

Now we turn to the experimental observation of intersubband transitions in van der Waals quantum wells. We specifically chose exfoliated TMD flakes that consist of terraces (Fig. 2) to compare the optical response of quantum wells of different thicknesses within the same flake. It is highly challenging to observe intersubband transitions in these flakes using conventional far-field illumination^{9,34} because the lateral size of each terrace with a constant thickness is smaller than the infrared diffraction limit, and intersubband transitions only couple to light with an out-of-plane polarization component. To overcome these challenges, we used s-SNOM and exploited the fact that exfoliated 2D materials naturally form a bare quantum well. The s-SNOM consists of a metallized atomic force microscope (AFM) tip that is illuminated by a continuous-wave laser source. The nanoscale concentrated infrared field (hot spot) that is generated around the tip apex interacts in the near field with the TMD flake underneath the tip. Importantly, the hot spot—of about 20 nm in diameter—contains out-of-plane polarization components and

can therefore excite intersubband transitions inside the TMD flake. We collect the light scattered back by the tip, which carries (quantitative) information about the sample's complex permittivity and thus its absorption at the illumination photon energy E_{ph} . This allows us to resolve intersubband transitions spatially with an unprecedented resolution of 20 nm and a sensitivity high enough to detect the intersubband transition of about a single electron (on average) under the AFM tip. By combining interferometric and tip-modulated detection (Fig. 2a), we record a complex scattered optical signal s_3 at the third harmonic of the AFM tip oscillation frequency f_{tip} , whose absolute value $|s_3|$ increases monotonically with N , and whose phase φ_3 is—in the case of weak resonances—proportional to the optical absorption of the TMD flake^{35–38} (Supplementary Section III). We use $|s_3|$ to identify N across the probed flake, as shown in Fig. 2b.

To isolate the absorption signal of intersubband transitions from the background signal and noise sources, such as laser and interferometer drifts, we modulated the charge carrier density of WSe₂ by applying a square wave backgate voltage V_{BG} between the Si wafer and two Cr/Au contacts evaporated on the TMD flake (Fig. 2c and Supplementary Section IV). Applying V_{BG} modulates the doping of the WSe₂ flake between charge neutrality and p-doping, which populates the first subband in the valence band and allows the excitation of hole intersubband transitions. When scanning the AFM tip over a TMD flake with different N , we simultaneously monitored V_{BG} and the gate-induced change in the third harmonic phase signal ($\Delta\varphi_3$) and extracted the change of absorption of the WSe₂ flake induced by a change in carrier density, as shown in Fig. 2d. We note that this gate-modulation technique improves the signal/noise ratio, but the generally observed trends presented in this work are also visible without the modulation technique.

A spatial map of $\Delta\varphi_3$ for $E_{ph} = 117$ meV over an area of $13 \times 10 \mu\text{m}^2$ with a spatial resolution of ~ 20 nm is shown in Fig. 2e. A clearly enhanced absorption is observed in the area of the flake where $N=1$ and $N=5$. When repeating the same scan at $E_{ph} = 165$ meV, we only observed absorption in the area where $N=4$ (Fig. 2f). This distinct behaviour originates from two different absorption contributions. (1) We attribute the enhanced absorption of the $N=4$ and $N=5$ regions of the flake to intersubband transitions. Comparing the observed absorption energies with the ab initio calculations from Fig. 1g, we find that hole intersubband transitions occur at energies close to 165 and 117 meV for WSe₂ flakes with $N=4$ and $N=5$, respectively. Therefore, these spatial absorption maps are a first indication that we observed intersubband transitions. (2) The absorption in the monolayer region at $E_{ph} = 117$ meV is attributed to Drude absorption: as the charge carriers induced by the applied V_{BG} are confined within a single atomic layer, the absorption due to free charge carriers is much higher than in the few-layer regions, where the same number of charge carriers is distributed over several layers (Supplementary Section V). Thus, the relative contribution of Drude absorption is larger in the monolayer region.

Spectrally resolved absorption measurements

To corroborate our interpretation, we spectrally resolved the intersubband resonances by changing E_{ph} in small steps. We averaged the recorded optical signals s_3 over the areas of the flake with a constant thickness. Due to the interferometric detection, s_3 is a complex signal and allows us to recover both the real and imaginary part of the relative permittivity of WSe₂, ϵ_{WSe_2} , by using a thin-film inversion model (Supplementary Section III)^{37,38}. We note that the flake thickness, the effect of the substrate and the different measurement parameters, such as tapping amplitude and demodulation order, are accounted for by the inversion model, but the qualitative resonance features are directly visible in the raw data. Figure 3a shows both $\Delta\varphi_3$ and the obtained $\text{Im}(\epsilon_{WSe_2})$ when the WSe₂ flake is p-doped, assuming $\text{Im}(\epsilon_{WSe_2})=0$ for charge-neutral WSe₂ in the infrared frequency range. First, we identified a general decrease of $\text{Im}(\epsilon_{WSe_2})$

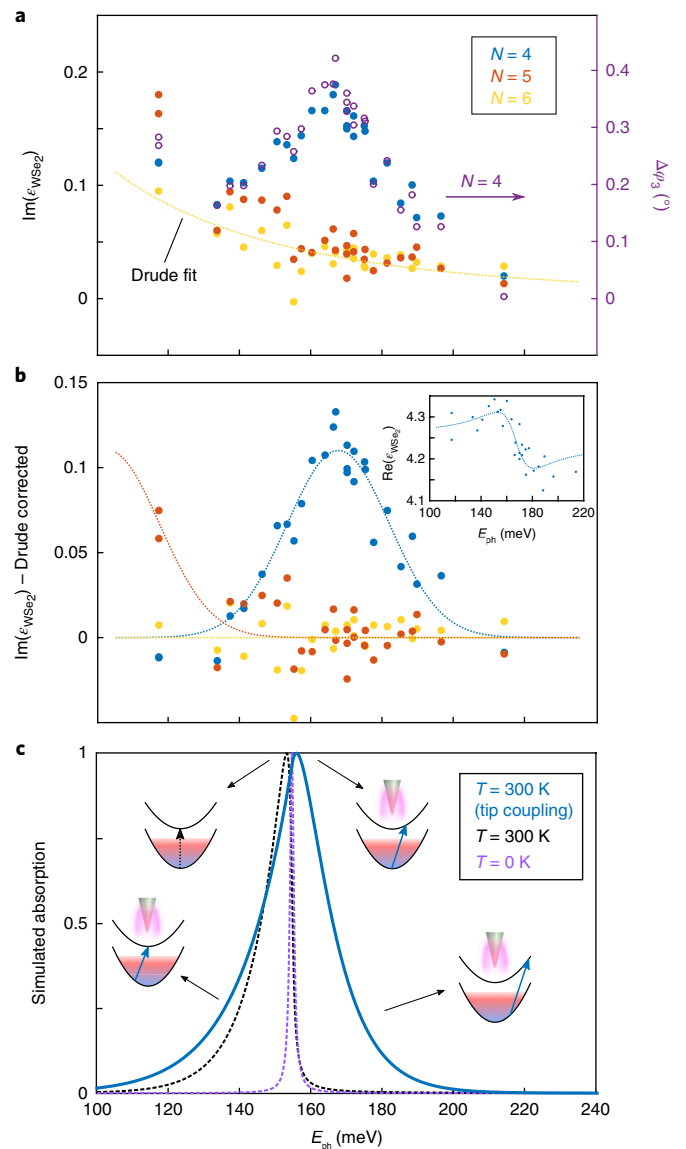


Fig. 3 | Intersubband absorption spectra in few-layer WSe₂.

a, Experimentally obtained $\text{Im}(\epsilon_{WSe_2})$ (filled dots) for different excitation photon energies E_{ph} and layer numbers N . $\text{Im}(\epsilon_{WSe_2})$ was calculated from the measured optical signals using a thin-film inversion model^{37,38}. The measurement was performed for a hole concentration $n_{2D} \approx 9 \times 10^{11} \text{ cm}^{-2}$. The yellow dotted line is a Drude fit to the $N=6$ data. To demonstrate that the intersubband resonance for $N=4$ is also visible in the raw data, we show $\Delta\varphi_3$ for $N=4$ (open circles) **b**, Same data as in **a** with the Drude contribution subtracted. The blue dotted line shows a Gaussian fit to the $N=4$ intersubband resonance, which yields a centre energy of 167.5 ± 1.5 meV and linewidth $\Gamma = 33 \pm 4$ meV. The orange dotted line is a Gaussian guide to the eye for the $N=5$ intersubband resonance, assuming the same tip-induced Γ . Inset: $\text{Re}(\epsilon_{WSe_2})$ for the $N=4$ area of the flake. The dotted line is a guide to the eye for a Lorentzian resonance. **c**, Absorption line shapes obtained from ab initio calculations. Calculations were done for low carrier concentrations (Boltzmann distribution) at the Γ point of a p-doped 2H-WSe₂ crystal with $N=4$ (Supplementary Section II). The solid blue line shows the expected line shape for transitions excited by the near field around an AFM tip with a radius of 12 nm at room temperature. The line shape is broadened and blueshifted compared to far-field excitations with negligible in-plane momentum, shown as dashed lines for $T=300$ K (black) and $T \approx 0$ K (purple). Insets illustrate the possible transitions from the first to the second subband. The two subbands exhibit slightly different effective masses.

with E_{ph} for all layer thicknesses. We attribute this behaviour to Drude absorption of holes that we account for (Supplementary Section V) by a standard complex Drude term $\epsilon_{\text{Drude}}(\omega) = -\frac{D}{\omega\epsilon_0 i\tau^{-1} + \omega}$, with the vacuum permittivity ϵ_0 , the Drude weight D , scattering time τ and $E_{\text{ph}} = \hbar\omega$. To address quantitatively the intersubband absorption resonances, we subtract the Drude contribution from the obtained $\text{Im}(\epsilon_{\text{WSe}_2})$ (Fig. 3b). We clearly distinguish an absorption peak for $N=4$, as well as enhanced absorption for $N=5$ at low photon energies. A Gaussian fit to the $N=4$ data yields a centre energy of 167.5 ± 1.5 meV and a full-width at half-maximum $\Gamma = 33 \pm 4$ meV. The obtained $\text{Re}(\epsilon_{\text{WSe}_2})$ shows a resonance behaviour at the same energy, which supports our conclusion that we observed a resonant absorption. The experimentally observed resonance energy (168 meV) is slightly higher than the theoretical predictions (145 and 154 meV for the two DFT calculations), which may be due to many-body effects³⁹ and corrections due to interactions with the electron or hole plasma⁴⁰.

We proceed with discussing the linewidth of the intersubband transitions. As 2D materials have atomically smooth surfaces, we expect that the linewidth of van der Waals quantum wells is not significantly broadened by interface roughness scattering, which is a dominant broadening mechanism in III–V semiconductor quantum wells^{41,42}. However, the linewidth can be broadened by both phonons or disorder. We calculate the optical-phonon-limited linewidth at low temperatures to be 0.66 meV and therefore much smaller than it is in epitaxial quantum wells⁴¹. At room temperature, the calculated linewidth $\Gamma \approx 5.9$ meV is much larger, which originates from the differences in the in-plane effective masses in the different subbands. The holes in the second subband are heavier than those in the first subband, which spreads the absorption for high temperatures or strongly doped films to $\Gamma \approx \left(1 - \frac{m_1}{m_2}\right) \max\{\epsilon_F, k_B T \log 2\}$, where m_1 and m_2 are the in-plane masses in the first and second subbands, respectively, $m_i^{-1} = m_{\text{xy}}^{-1} \left(1 + \frac{\pi^2 \zeta}{(N+2n)^2 \epsilon^2}\right)$, where the difference is determined by the non-parabolicity in the dispersion of holes in the bulk crystal, ϵ_F is the Fermi energy, k_B is Boltzmann's constant and T is the temperature (Supplementary Section II gives more details). The measured linewidth of $\Gamma = 33$ meV is larger than these theoretical estimates for the intrinsic linewidth. An additional broadening mechanism in our experiment stems from the sharpness of the AFM tip, which provides momentum for non-vertical transitions. To quantify this, we examined in more detail the hot spot around the AFM tip apex that excites intersubband transitions. The in-plane momenta that contribute to the near-field coupling are given by a broad bell-shaped function (Supplementary Section II), which peaks at a \mathbf{k} -vector that is inversely related to the tip curvature^{43,44}. Due to this broad momentum distribution, a wide range of non-vertical transitions with finite momentum transfer and a distribution of transition energies contribute to the signal. This leads to a broadening and blue shift of the absorption line shape. The sharpest features around the AFM tip apex determine the in-plane momentum distribution and are typically around 12 nm for the used AFM tips. Calculations for this tip radius yield $\Gamma = 24$ meV (Fig. 3c), which indicates that tip-induced broadening plays an important role for the experimentally observed linewidth. However, we cannot exclude additional contributions to the linewidth broadening caused by disorder. We note that we did not observe signatures of spatial disorder in our spatially resolved measurements (Supplementary Section VI).

Doping dependence and ambipolar absorption

Another key signature of intersubband transitions is the dependence of the sheet absorption α on the carrier density n_{2D} . α is typically obtained in far-field absorption measurements^{9,34}. For an ideal, infinitely deep quantum well, assuming parallel subbands and $T = 0$ K, calculations yield $\alpha = n_{2D} \frac{e^2 \hbar f_{12}}{\epsilon \epsilon_m \Gamma}$, with the electron charge e , speed of light c , oscillator strength $f_{12} = 0.96$ for the transition from the first to the second subband and ϵ the static out-of-plane permittivity. To experimentally study this dependence, we varied n_{2D} by

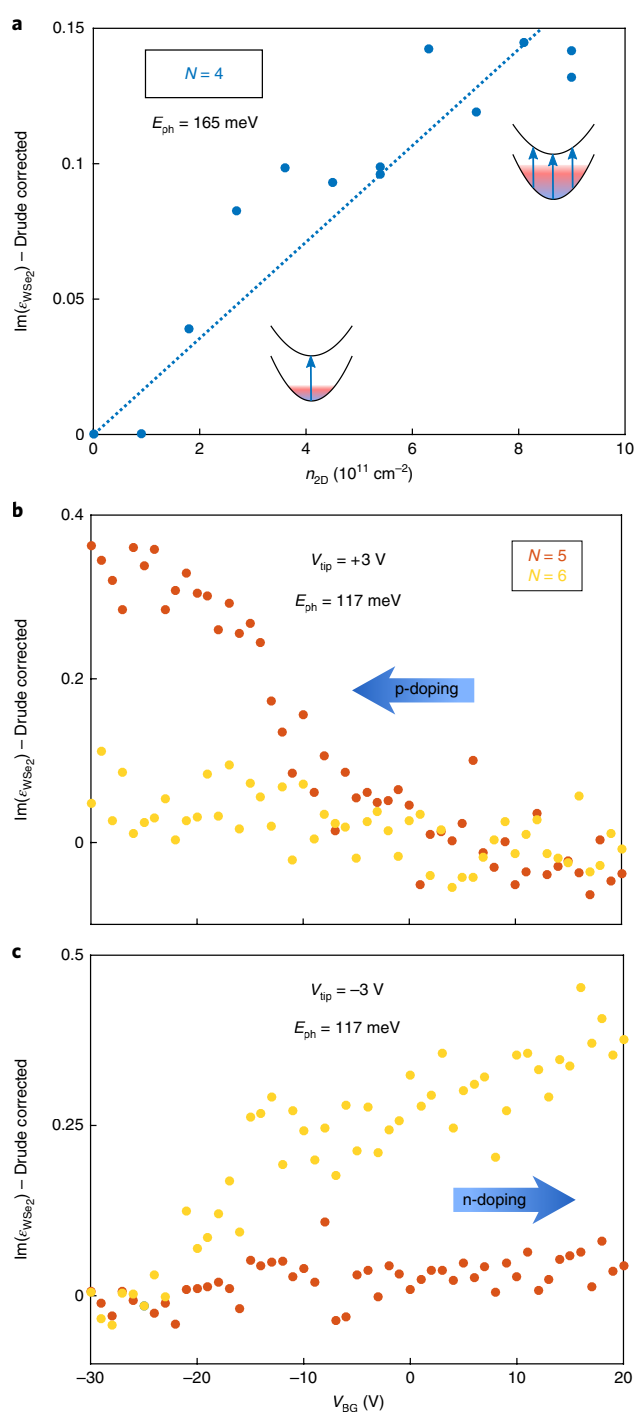


Fig. 4 | Doping dependence of electron and hole intersubband absorption. **a**, Drude corrected $\text{Im}(\epsilon_{\text{WSe}_2})$ for different hole densities n_{2D} . The measurement was done at $E_{\text{ph}} = 165$ meV, which corresponds to the centre of the $N=4$ intersubband resonance. The carrier concentration was controlled by varying the maximum voltage $V_{\text{BG,max}}$ of the square wave function applied to the backgate. Insets show possible transitions for low and high carrier densities. **b, c**, Observation of hole ($N=5$) (**b**) and electron ($N=6$) (**c**) intersubband transitions within the same WSe_2 flake at $E_{\text{ph}} = 117$ meV. Shown is the Drude corrected $\text{Im}(\epsilon_{\text{WSe}_2})$. The d.c. backgate voltage V_{BG} was increased stepwise from -30 to $+20$ V. The measurement was performed on a WSe_2 flake on top of a SiO_2 substrate. To reach higher doping levels, an additional d.c. voltage V_{tip} was applied between the WSe_2 flake and the AFM tip, which locally induced holes for $V_{\text{tip}} = +3$ V (**b**) or electrons for $V_{\text{tip}} = -3$ V (**c**) due to capacitive interactions with the metallized, grounded AFM tip.

changing the modulation amplitude of the backgate voltage, $V_{\text{BG,max}}$ at $E_{\text{ph}} = 165 \text{ meV}$, which corresponds to the centre energy of the $N=4$ intersubband resonance. The measured (Drude-corrected) $\text{Im}(\epsilon_{\text{WSe}_2})$ as a function of $n_{2\text{D}}$, shown in Fig. 4a, displays a monotonic increase of the absorption with $n_{2\text{D}}$. This is consistent with the idealized square well model, although we note that the exact function of the increase might be affected by possible contributions from many-body effects and non-parabolic bands. Experimentally, we found for the highest hole density ($n_{2\text{D}} = 9 \times 10^{11} \text{ cm}^{-2}$, extracted from capacitance measurements on a separate device) a maximum absorption of $\alpha_{\text{exp}} = 0.017 \pm 0.002\%$, which we calculated from the measured complex value of ϵ_{WSe_2} (Supplementary Section VIII). This is in good agreement with the idealized model, which yields $\alpha = 0.026\%$ for a WSe_2 crystal with $N=4$ taking into account the measured linewidth $\Gamma = 33 \text{ meV}$. We note that the absorption will be significantly enhanced with narrower linewidths, reaching values as high as $\alpha = 1.3\%$ for the phonon-limited linewidth $\Gamma = 0.66 \text{ meV}$.

We further demonstrated the versatility of 2D materials by ambipolar electrical control of the intersubband transitions in the valence and conduction bands. We tuned the carrier density from the p-doped to the n-doped regime and observed intersubband transitions in both cases. Interestingly, at $E_{\text{ph}} = 117 \text{ meV}$, these transitions occur for different layer thicknesses. As we have seen before, we observed hole intersubband transitions in the $N=5$ area of the flake (Fig. 4b). However, when the flake is n-doped, we observed enhanced absorption due to electron intersubband transitions in the $N=6$ region of the flake (Fig. 4c). This observation is in excellent agreement with our theoretical ab initio calculations, in which the electron transitions for a given E_{ph} occur in a thicker part of the flake than the hole transitions (Fig. 1f,g). We note that to reach n- and p-doping without leakage through the underlying oxide we use the AFM tip to induce additional doping to the flake (Supplementary Section VII).

Conclusions

We report the experimental observation of intersubband transitions in few-layer WSe_2 crystals with spatially and spectrally resolved measurements supported by detailed ab initio calculations. The obtained spatial resolution of 20 nm cannot be achieved by classical far-field measurements. Intersubband transitions are not unique to WSe_2 ; they can be found in any gapped 2D material (Supplementary Section IX shows similar measurements on MoS_2). In a future study, the role of disorder and many-body interactions needs to be investigated more thoroughly to provide conclusions on the intrinsic linewidth. Recently, wafer-scale multilayer TMD flakes became commercially available and progress is being made to reduce the defect density in these large-area films⁴⁵. This also provides the opportunity to study intersubband transitions in the far field and is promising for future experiments and applications. Our study offers a glimpse of the physics and technology potentially enabled by van der Waals quantum wells, such as infrared detectors, sources and lasers with the potential for compact integration with Si integrated circuits. Particularly appealing is the possibility of combining^{14,46} van der Waals quantum wells with any of the wide variety of different 2D crystals, which include semimetals, dielectrics, topological insulators^{47,48}, superconductors⁴⁹ and ferromagnets^{50,51}, with freedom to choose the relative lattice alignment angle between different layers. This allows for unprecedented freedom in designing novel optoelectronic devices with phenomena and functionalities that are not accessible with bulk materials.

Code availability. The code used to process the raw data of this study are available from the corresponding author upon request.

Data availability. The raw data of this study are available from the corresponding author upon request.

Received: 23 March 2018; Accepted: 16 July 2018;
Published online: 27 August 2018

References

- Kroemer, H. Nobel lecture: Quasi-electric fields and band offset: teaching electrons new tricks. *Rev. Mod. Phys.* **73**, 783–793 (2001).
- Alferov, Z. I. Nobel lecture: The double heterostructure concept and its applications in physics, electronics, and technology. *Rev. Mod. Phys.* **73**, 767–782 (2001).
- Hayashi, I., Panish, M. B., Foy, P. W. & Sumski, S. Junction lasers which operate continuously at room temperature. *Appl. Phys. Lett.* **17**, 109–111 (1970).
- Nakamura, S., Mukai, T. & Senoh, M. Candela-class high-brightness InGaN/AlGaIn double-heterostructure blue-light-emitting diodes. *Appl. Phys. Lett.* **64**, 1687–1689 (1994).
- Bhattacharya, P. & Mi, Z. Quantum-dot optoelectronic devices. *Proc. IEEE* **95**, 1723–1740 (2007).
- Wang, J., Gudiksen, M. S., Duan, X., Cui, Y. & Lieber, C. M. Highly polarized photoluminescence and photodetection from single indium phosphide nanowires. *Science* **293**, 1455–1457 (2001).
- Levine, B. F. Quantum well infrared photodetectors. *J. Appl. Phys.* **74**, R1–R81 (1993).
- Faist, J. et al. Quantum cascade laser. *Science* **264**, 553–556 (1994).
- West, L. C. & Eglash, S. J. First observation of an extremely large-dipole infrared transition within the conduction band of a GaAs quantum well. *Appl. Phys. Lett.* **46**, 1156–1158 (1985).
- Helm, M. Intersubband semiconductor light sources: history, status, and future. In *Infrared and Millimeter Waves, Conference Digest of the 2004 Joint 29th International Conference on 2004 and 12th International Conference on Terahertz Electronics* (IEEE, 2004).
- Liu, H. C., & Capasso, F. *Intersubband Transitions in Quantum Wells: Physics and Device Applications* (Elsevier, Amsterdam, 1999).
- Warwick, C. A., Jan, W. Y., Ourmazd, A. & Harris, T. D. Does luminescence show semiconductor interfaces to be atomically smooth? *Appl. Phys. Lett.* **56**, 2666–2668 (1990).
- Novoselov, K. S. et al. Two-dimensional atomic crystals. *Proc. Natl Acad. Sci. USA* **102**, 10451–10453 (2005).
- Novoselov, K. S., Mishchenko, A., Carvalho, A. & Castro Neto, A. H. 2D materials and van der Waals heterostructures. *Science* **353**, 461 (2016).
- Mak, K. F. & Shan, J. Photonics and optoelectronics of 2D semiconductor transition metal dichalcogenides. *Nat. Photon.* **10**, 216–226 (2016).
- Wang, Q. H., Kalantar-Zadeh, K., Kis, A., Coleman, J. N. & Strano, M. S. Electronics and optoelectronics of two-dimensional transition metal dichalcogenides. *Nat. Nanotech.* **7**, 699–712 (2012).
- Koppens, F. H. L. et al. Photodetectors based on graphene, other two-dimensional materials and hybrid systems. *Nat. Nanotech.* **9**, 780–793 (2014).
- Cui, X. et al. Multi-terminal transport measurements of MoS_2 using a van der Waals heterostructure device platform. *Nat. Nanotech.* **10**, 534–540 (2015).
- Xu, S. et al. Odd-integer quantum Hall states and giant spin susceptibility in p-type few-layer WSe_2 . *Phys. Rev. Lett.* **118**, 067702 (2017).
- Bandurin, D. A. et al. High electron mobility, quantum Hall effect and anomalous optical response in atomically thin InSe. *Nat. Nanotech.* **12**, 223–227 (2017).
- Schaibley, J. R. et al. Valleytronics in 2D materials. *Nat. Rev. Mater.* **1**, 1–15 (2016).
- Mak, K. F., McGill, K. L., Park, J. & McEuen, P. L. The valley Hall effect in MoS_2 transistors. *Science* **344**, 1489–92 (2014).
- Back, P., Zeytinoglu, S., Ijaz, A., Kroner, M. & Imamoglu, A. Realization of an electrically tunable narrow-bandwidth atomically thin mirror using monolayer MoSe_2 . *Phys. Rev. Lett.* **120**, 037401 (2018).
- Scuri, G. et al. Large excitonic reflectivity of monolayer MoSe_2 encapsulated in Hexagonal Boron Nitride. *Phys. Rev. Lett.* **120**, 037402 (2018).
- Cadiz, F. et al. Excitonic linewidth approaching the homogeneous limit in MoS_2 -based van der Waals heterostructures. *Phys. Rev. X* **7**, 021026 (2017).
- Ajayi, O. A. et al. Approaching the intrinsic photoluminescence linewidth in transition metal dichalcogenide monolayers. *2D Mater.* **4**, 031011 (2017).
- Wang, L. et al. One-dimensional electrical contact to a two-dimensional material. *Science* **342**, 614–7 (2013).
- Britnell, L. et al. Field-effect tunneling transistor based on vertical graphene heterostructures. *Science* **335**, 947–950 (2012).
- Keilmann, F. & Hillenbrand, R. Near-field microscopy by elastic light scattering from a tip. *Phil. Trans. R. Soc. A* **362**, 787–805 (2004).
- Ruiz-Tijerina, D. A., Danovich, M., Yelgel, C., Zolyomi, V. & Fal'ko, V. Hybrid $\mathbf{k}\cdot\mathbf{p}$ tight-binding model for subbands and infrared intersubband optics in few-layer films of transition metal dichalcogenides: MoS_2 , MoSe_2 , WS_2 , and WSe_2 . *Phys. Rev. B* **98**, 035411 (2018).
- Kormanyos, A. et al. $\mathbf{k}\cdot\mathbf{p}$ theory for two-dimensional transition metal dichalcogenide semiconductors. *2D Mater.* **2**, 22001 (2014).
- Sahin, H. et al. Anomalous Raman spectra and thickness-dependent electronic properties of WSe_2 . *Phys. Rev. B* **87**, 165409 (2013).
- Huang, W., Luo, X., Gan, C. K., Quek, S. Y. & Liang, G. Theoretical study of thermoelectric properties of few-layer MoS_2 and WSe_2 . *Phys. Chem. Chem. Phys.* **16**, 10866 (2014).

34. Kane, M. J., Emeny, M. T., Apsley, N., Whitehouse, C. R. & Lee, D. Inter-sub-band absorption in GaAs/AlGaAs single quantum wells. *Semicond. Sci. Technol.* **3**, 722–725 (1988).
35. Huth, F. et al. Nano-FTIR absorption spectroscopy of molecular fingerprints at 20 nm spatial resolution. *Nano Lett.* **12**, 3973–3978 (2012).
36. Taubner, T., Hillenbrand, R. & Keilmann, F. Nanoscale polymer recognition by spectral signature in scattering infrared near-field microscopy. *Appl. Phys. Lett.* **85**, 5064–5066 (2004).
37. Govyadinov, A. A., Amenabar, I., Huth, F., Carney, P. S. & Hillenbrand, R. Quantitative measurement of local infrared absorption and dielectric function with tip-enhanced near-field microscopy. *J. Phys. Chem. Lett.* **4**, 1526–1531 (2013).
38. Govyadinov, A. A. et al. Recovery of permittivity and depth from near-field data as a step toward infrared nanotomography. *ACS Nano* **8**, 6911–6921 (2014).
39. Manasreh, M. O. et al. Origin of the blueshift in the intersubband infrared absorption in GaAs/Al_{0.3}Ga_{0.7}As multiple quantum well. *Phys. Rev. B* **43**, 9996–9999 (1991).
40. Allen, S. J., Tsui, D. C. & Vinter, B. On the absorption of infrared radiation by electrons in semiconductor inversion layers. *Solid State Commun.* **88**, 425–428 (1993).
41. Unuma, T., Yoshita, M., Noda, T., Sakaki, H. & Akiyama, H. Intersubband absorption linewidth in GaAs quantum wells due to scattering by interface roughness, phonons, alloy disorder, and impurities. *J. Appl. Phys.* **93**, 1586–1597 (2003).
42. Tsujino, S. et al. Interface-roughness-induced broadening of intersubband electroluminescence in p-SiGe and n-GaInAs/AlInAs quantum-cascade structures. *Appl. Phys. Lett.* **86**, 062113 (2005).
43. Fei, Z. et al. Infrared nanoscopy of Dirac plasmons at the graphene–SiO₂ interface. *Nano Lett.* **11**, 4701–4705 (2011).
44. Kurman, Y. et al. Control of semiconductor emitter frequency by increasing polariton momenta. *Nat. Photon.* **12**, 423–429 (2018).
45. Edelberg, D. et al. Hundredfold enhancement of light emission via defect control in monolayer transition-metal dichalcogenides. Preprint at <https://arxiv.org/abs/1805.00127> (2018).
46. Geim, A. K. & Grigorieva, I. V. Van der Waals heterostructures. *Nature* **499**, 419–25 (2013).
47. Fei, Z. et al. Edge conduction in monolayer WTe₂. *Nat. Phys.* **13**, 677–682 (2017).
48. Wu, S. et al. Observation of the quantum spin Hall effect up to 100 Kelvin in a monolayer crystal. *Science* **359**, 76–79 (2018).
49. Xi, X. et al. Ising pairing in superconducting NbSe₂ atomic layers. *Nat. Phys.* **12**, 139–143 (2015).
50. Huang, B. et al. Layer-dependent ferromagnetism in a van der Waals crystal down to the monolayer limit. *Nature* **546**, 270–273 (2017).
51. Gong, C. et al. Discovery of intrinsic ferromagnetism in two-dimensional van der Waals crystals. *Nature* **546**, 265–269 (2017).
52. Ocelic, N., Huber, A. & Hillenbrand, R. Pseudoheterodyne detection for background-free near-field spectroscopy. *Appl. Phys. Lett.* **89**, 101124 (2006).

Acknowledgements

We acknowledge discussions with A. Tredicucci about the general concept and S. Wall about the experimental measurement technique. We also thank A. Govyadinov for discussions about the thin-film inversion model. P.S. acknowledges financial support by a scholarship from the 'la Caixa' Banking Foundation. F.V. acknowledges financial support from Marie-Curie International Fellowship COFUND and ICFOnest programme. M.M. thanks the Natural Sciences and Engineering Research Council of Canada (PGSD3-426325-2012). K.-J.T. acknowledges support from a Mineco Young Investigator Grant (FIS2014-59639-JIN). F.H.L.K. acknowledges financial support from the Government of Catalonia through an SGR grant (2014-SGR-1535), and from the Spanish Ministry of Economy and Competitiveness through the 'Severo Ochoa'; Programme for Centres of Excellence in R&D (SEV-2015-0522), support by the Fundacio Cellex Barcelona, CERCA Programme/Generalitat de Catalunya and the Mineco grants Ramón y Cajal (RYC-2012-12281) and Plan Nacional (FIS2013-47161-P and FIS2014-59639-JIN). Furthermore, the research leading to these results received funding from the European Union Seventh Framework Programme under grant agreement no. 696656 Graphene Flagship, European Research Council (ERC) Starting grant (307806, CarbonLight) and ERC Synergy Grant Hetero2D. K.S.T. acknowledges financial support from The Center for Nanostructured Graphene sponsored by the Danish National Research Foundation (Project DNRF103) and the ERC under the European Union's Horizon 2020 research and innovation programme (grant agreement no. 773122, LIMA).

Author contributions

P.S., S.L., K.S.T. and F.H.L.K. conceived and designed the experiment. P.S. and S.M. carried out the experiment. P.S. fabricated the samples and performed the data analysis. G.N. provided assistance in the sample fabrication. P.S., F.V., M.M., K.-J.T. and F.H.L.K. interpreted the results. S.L., M.D., D.A.R.-T., C.Y., V.F. and K.S.T. developed the theoretical calculations for intersubband transitions. P.S., F.V., S.L., M.M., K.-J.T., M.D., D.A.R.-T., C.Y., V.F., K.S.T., R.H. and F.H.L.K. co-wrote the manuscript. All the authors contributed to discussions of the manuscript.

Competing interests

R.H. is cofounder of and on the scientific advisory board of Neaspec GmbH, a company that produces scattering-type near-field scanning optical microscope systems, such as the one used in this study. The remaining authors declare no competing interests.

Additional information

Supplementary information is available for this paper at <https://doi.org/10.1038/s41565-018-0233-9>.

Reprints and permissions information is available at www.nature.com/reprints.

Correspondence and requests for materials should be addressed to F.H.L.K.

Publisher's note: Springer Nature remains neutral with regard to jurisdictional claims in published maps and institutional affiliations.